Report

Current Biology

Desmosomal Junctions Govern Tissue Integrity and Actomyosin Contractility in Apoptotic Cell Extrusion

Highlights

- Desmosomal junctions (DJs) remains intact during apoptotic cell extrusion
- Neighboring non-dying cells possess two DJs in the middle of cell extrusion
- Depletion of desmoplakin leads to a failure of cell extrusion
- DJs govern actomyosin contractility in static epithelium and apoptotic cell extrusion

Authors

Minnah Thomas, Benoit Ladoux, Yusuke Toyama

Correspondence

dbsty@nus.edu.sg

In Brief

Thomas et al. show pivotal role of desmosomal junction in governing actomyosin contractility and maintenance of epithelial sheet integrity during apoptotic cell extrusion. We speculate that desmoplakin-depleted tissues could lead to pathological conditions through defective actomyosin contractility and/or apoptotic cell clearance.

Thomas et al., 2020, Current Biology *30*, 682–690
February 24, 2020
https://doi.org/10.1016/j.cub.2020.01.002

CellPress

CellPress

Current Biology
Report

Desmosomal Junctions Govern Tissue Integrity and Actomyosin Contractility in Apoptotic Cell Extrusion

Minnah Thomas,[1] Benoit Ladoux,[2] and Yusuke Toyama[1,3,4,*]
[1]Mechanobiology Institute, Singapore, Level 5, T-lab Building, 5A Engineering Drive 1, Singapore 117411, Singapore
[2]Université de Paris, CNRS, Institut Jacques Monod, 15 rue Hélène Brion, 75013 Paris, France
[3]Department of Biological Sciences, National University of Singapore, 14 Science Drive 4, Singapore 117543, Singapore
[4]Lead Contact
*Correspondence: dbsty@nus.edu.sg
https://doi.org/10.1016/j.cub.2020.01.002

SUMMARY

During apoptosis, or programmed cell death, a dead cell could be expelled from the tissue by coordinated processes between the dying cell and its neighbors. Apoptotic cell extrusion is driven by actomyosin cable formation and its contraction and lamellipodial crawling of the neighboring cells [1–4]. Throughout cell extrusion, the mechanical coupling of epithelia needs to be maintained in order to preserve tissue homeostasis [1]. Although much is known about the regulation of adherens junctions (AJs) in apoptotic cell extrusion [4–7], the role and dynamics of desmosomal junctions (DJs) during this process remain poorly understood. Here, we show that DJs stay intact throughout and are crucial for cell extrusion. Pre-existing DJs between the apoptotic cell and neighboring cells remain intact, even during the formation of *de novo* DJs between non-dying cells, suggesting the neighboring cells possess two DJs in the middle of apoptotic cell extrusion. We further found that an actomyosin cable formed in the vicinity of DJs upon apoptosis and subsequently deviated from DJs during its constriction. Interestingly, the departure of the actomyosin cable from DJs coincided with the timing when DJs lost their straightness, suggesting a release of junctional tension at DJs and a mechanical coupling between DJs and actomyosin contractility. The depletion of desmoplakin resulted in defective contractility and an inability to form *de novo* DJs, leading to a failure of apoptotic cell extrusion. Our study provides a framework to explain how desmosomes play pivotal roles in maintaining epithelial sheet integrity during apoptotic cell extrusion.

RESULTS AND DISCUSSION

During apoptotic cell extrusion, adherens junction components, including E-cadherin and α- and β-catenins, display a reduction in their levels at the interface between the apoptotic cell and neighboring cells. This reduction coincides with membrane disengagement, actomyosin cable formation, and relaxation of tissue tension [4]. Here, we investigate the dynamics of desmosomal junctions (DJs), which are a part of the tripartite epithelial junctions known to influence dynamic processes, such as collective cell migration [8] and skin differentiation [9, 10], during cell extrusion.

Desmosomal Junctions Stay Intact throughout Apoptotic Cell Extrusion

To understand how DJs were remodeled during the course of apoptotic cell extrusion, we used a UV laser to induce DNA damage and subsequent apoptotic cell extrusion (STAR Methods) [3] and followed the progression of extrusion using confocal microscopy (Figures 1A and S1A–S1C; Video S1). We first examined the distribution of desmoglein, one of the two cadherin types found in DJs, by expressing EGFP-tagged desmoglein 2 in wild-type (WT) Madin-Darby canine kidney (MDCK) cells (Figures 1B, S1D, and S1E). We took advantage of the non-homogeneous expression of desmoglein 2-FLAG-EGFP within a tissue and induced apoptosis in a non-EGFP-expressing cell that was adjacent to EGFP-positive cells in order to follow the changes in desmoglein in the neighboring non-dying cells. Stills from time-lapse videos showed that, in contrast to AJs (Figures S1F and S1G) [4], DJs between apoptotic and neighboring non-dying cells did not show a reduction in desmoglein 2 levels throughout extrusion (red arrows in Figure 1B; Video S1) but rather exhibited up to a 2.2- ± 0.5-fold increase in intensity (STAR Methods; Figure 1C). Furthermore, neighboring non-apoptotic cells formed punctate *de novo* DJs at the basal section of the cell, once lamellipodia formed in neighboring cells apposed to each other (blue arrows in Figures 1B and S1H). This was seen more clearly in the transverse view (Figure 1D), which shows a pre-existing DJ located at the lateral section of the cells (red arrows) and a nascent DJ with the new neighboring cell, formed at the tip of lamellipodia (blue arrows). Later, these *de novo* DJs became matured junctional plaques that are positioned more apically on the lateral membrane, suggesting the neighboring non-dying cells form mature DJs underneath the apically extruding apoptotic cell. We further noticed that DJs lost their straightness at later stages of cell extrusion (red arrows in Figure 1B; see also later section). A similar localization was

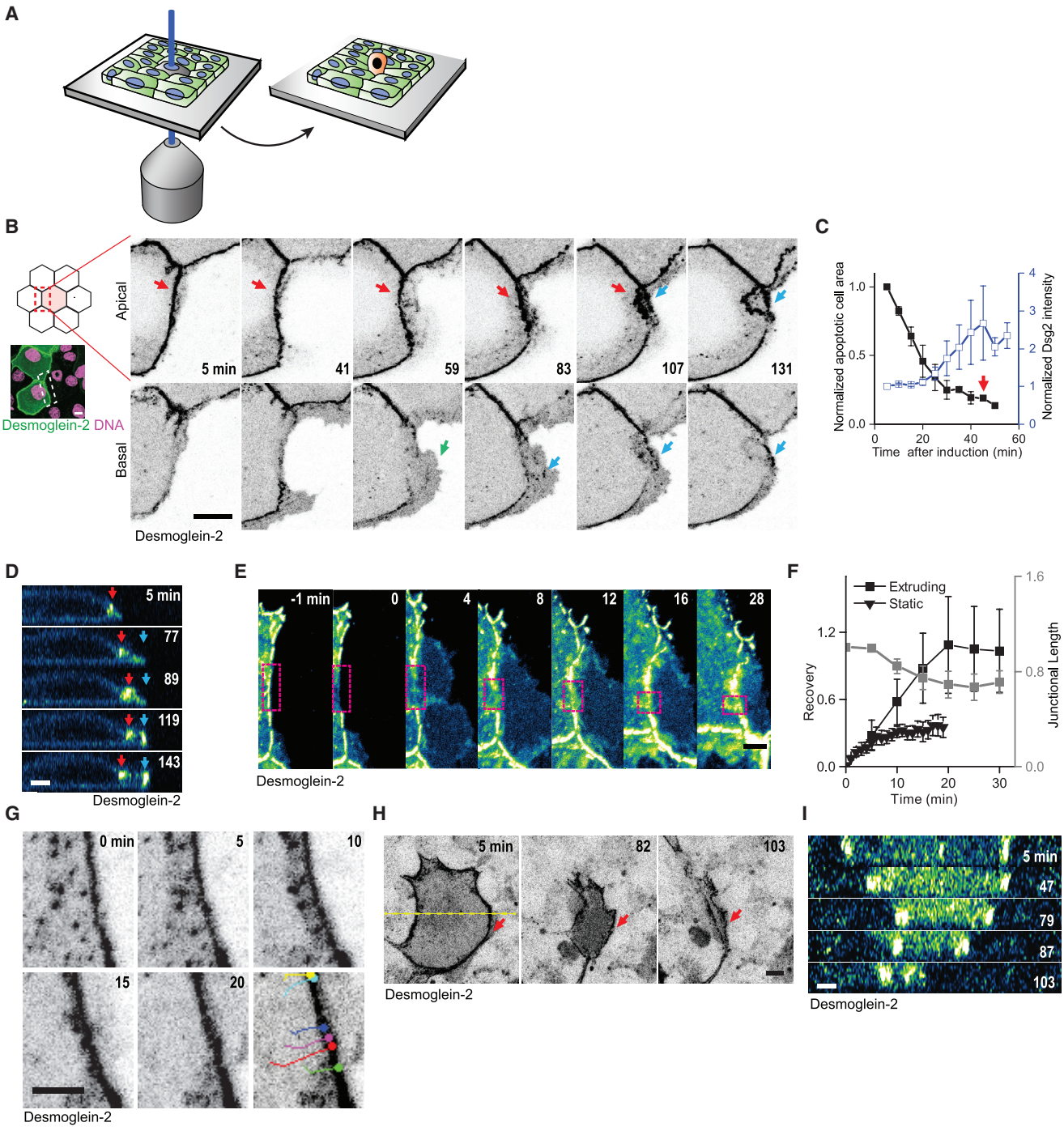

Figure 1. Desmosome Dynamics during Apoptotic Cell Extrusion

(A) Diagram illustrating the experimental setup for targeted apoptosis induction in MDCK monolayers.

(B) Confocal images showing DJ dynamics at apical (top panel) and basal (bottom panel) sections of the cell. Red, blue, and green arrows indicate the pre-existing DJ, *de novo* DJ, and lamellipodia, respectively. The survey view (left) of the extrusion site containing the region of interest (ROI) (white dotted box) used in (B) is shown. See also Figure S1 and Video S1.

(C) Graphs plotting normalized apoptotic cell area (black) and DJ intensity (blue) during extrusion (n = 6 independent experiments). The red arrow indicates the average extrusion time.

(D) Transverse view of a neighboring cell showing DJ dynamics during extrusion. Red and blue arrows indicate pre-existing and *de novo* DJs, respectively.

(E) Time-lapse images showing photobleaching and recovery (ROI: magenta box) of desmoglein 2 during extrusion. See also Figure S2.

(F) Graphs plotting normalized recovery curves of desmoglein 2 (black square) after photobleaching and corresponding junctional length (gray) during early apoptotic cell extrusion. The normalized recovery curve of desmoglein 2 in the non-apoptotic static junction (black triangle) is also shown for comparison (n = 5 independent experiments each). See also Figure S2.

(legend continued on next page)

observed in the endogenous desmosome during extrusion (Figure S1I) and during reactive oxygen species (ROS)-induced apoptosis (Figures S1J–S1L).

To understand whether pre-existing DJs are dynamic during extrusion, we performed fluorescence recovery after photobleaching (FRAP) of EGFP-tagged desmoglein 2 expressed in non-apoptotic cells at different stages of extrusion, classed as before, early, and late (i.e., after DJs lost their straightness) stage of cell extrusion (Figures 1E and S2A–S2C). Although it is challenging to quantitatively interpret the recovery rate because of the shortening of DJs during constriction, there was a turnover of desmoglein 2 at DJs (Figures 1F and S2B), suggesting that pre-existing DJs are dynamic throughout apoptotic cell extrusion. This recovery and the subsequent increase in desmoglein 2 intensity during extrusion originated, in part, from the incorporation of desmoglein 2 puncta from the cytoplasm into the DJs (Figures 1G, S2D, and S2E; Video S1), which is analogous to a previous observation made during DJ formation [11]. In order to uncover whether the dynamic nature of DJs is crucial for cell extrusion, we prevented the turnover of DJs by pre-treating the tissue with GÖ6976, which is a protein kinase C (PKC) inhibitor that prevents the transformation of stable desmosomes into a "remodelable" state [12]. Under such conditions, extrusion was defective, i.e., more cells failed to successfully extrude within 2 h after UV irradiation (Figures S2F and S2G), indicating that desmosome remodeling is required for extrusion. Next, we examined DJs in the apoptotic cell by tracking desmoglein 2-FLAG-EGFP in a dying cell, surrounded by non-labeled neighbors. Although biochemical analysis of desmosomal cadherins has reported that they undergo both caspase- and matrix metalloprotease (MMP)-mediated cleavage [13–18], we did not observe a strong reduction in desmoglein 2 levels in the apoptotic cell throughout extrusion (Figures 1H and 1I). Together, our data showed that pre-existing DJs between apoptotic and neighboring cells remain intact, even during the formation of *de novo* DJs between non-dying cells, suggesting that the neighboring cells possess two DJs in the middle of apoptotic cell extrusion. This further raises the possibility of intercellular force transduction across the interface during extrusion.

Cytokeratin-18 in the Neighboring Cell Aligns and Accumulates during Cell Extrusion

Junctional remodeling is often accompanied by the reorganization of the associated cytoskeleton. Therefore, we examined the dynamics of the DJ-associated intermediate filament protein cytokeratin-18 (CK18) tagged with mEmerald (Figure 2A) during apoptotic cell extrusion. Similar to our desmoglein 2 experiments, we induced apoptosis in a non-fluorescent cell next to mEmerald-positive cells to follow the changes in cytokeratin within the neighboring non-dying cells. Stills from time-lapse videos showed that cytokeratin filaments that were linked to pre-existing DJs realigned toward the apoptotic cell during extrusion (Figures 2A, top, and S2H; Video S2). We then quantified the orientation of cytokeratin filaments by measuring the structure tensor of the image [19] (STAR Methods), which was represented as color-coded orientation plots (Figure 2C). The orientation of the filaments in the vicinity of DJs at the interface between dying and non-dying cells was random (i.e., mixed colors) at the early stage of extrusion and became more polarized (i.e., cold colors) toward the apoptotic cell at a late stage (Figures 2C and 2D). These observations were further supported by plotting the distribution of orientation angles of filaments (Figure 2E). Another pool of dynamic cytokeratin-18 was found within the lamellipodia formed in the neighboring cells (Figure 2A, white arrow). Quantitative measurement of the fluorescence intensity of cytokeratin-18 at the junctional interface within neighboring cells showed that the intensity increased as apoptotic cell extrusion progressed (Figure 2B). A similar accumulation of cytokeratin-18 was observed during extrusion in the endogenous protein (Figure 2F), and the accumulation of cytokeratin-5 and 8 has been reported in oncogenic cell extrusion [20]. To understand the kinetics of keratin reorganization in the course of extrusion, we took advantage of the photoconvertible protein, Dendra2-tagged cytokeratin-18, and performed photoconversion experiments in the neighboring cells. We found that the intensity of the red signal, which represents the photoconverted pre-existing keratin, did not change over time (Figures S2I–S2K). By contrast, the intensity of the green signal decreased upon photoconversion and increased as extrusion progressed, suggesting that new cytokeratin-18 was recruited in the vicinity of the interface between dying and non-dying cells (Figures S2I–S2K). Together, the alignment and accumulation of cytokeratin during apoptotic cell extrusion prompted us to speculate that the viscoelastic gel-like cytoplasm in neighboring cells undergoes stretching and thus remodels toward the extrusion site. To test this hypothesis, we performed laser ablation to assess the tension in keratin filaments during extrusion. The reoriented keratin filaments at the late phase of extrusion were associated with a significantly higher tension in comparison to the random keratin network at the early phase of constriction, as shown by the recoil velocity (0.17 ± 0.06 μm/s versus 0.07 ± 0.04 μm/s; Figures 2G and 2H; Video S2). This indicates that desmosome-coupled keratin network is stretched and DJs bear mechanical force during extrusion [21].

An Actomyosin Cable Forms in Close Proximity to the DJs at the Early Stage and Decouples from DJs at the Late Stage of Cell Extrusion

We next assessed the relationship between DJs and apoptosis-induced actomyosin cable formation by imaging LifeAct-Ruby (a marker for F-actin) and GFP-tagged desmoglein 2 (Figures 3A and 3B). Time-lapse confocal images showed that an apoptosis-associated actomyosin cable formed in close

(G) Confocal images showing the dynamics of desmoglein 2 cytoplasmic puncta toward DJs during early cell extrusion. The bottom panel shows the tracks of desmoglein 2 puncta over time (n = 5 independent experiments). See also Figure S2 and Video S1.

(H) Confocal images showing the temporal localization of desmoglein 2-FLAG-EGFP in the apoptotic cell during extrusion. Red arrows indicate a junctional interface (n = 5 independent experiments).

(I) Transverse view of apoptotic cell extrusion generated along the yellow dotted line highlighted in (H).

The data represented in (C) and (F) represent mean ± SEM. Scale bars, 5 μm except (H) (10 μm).

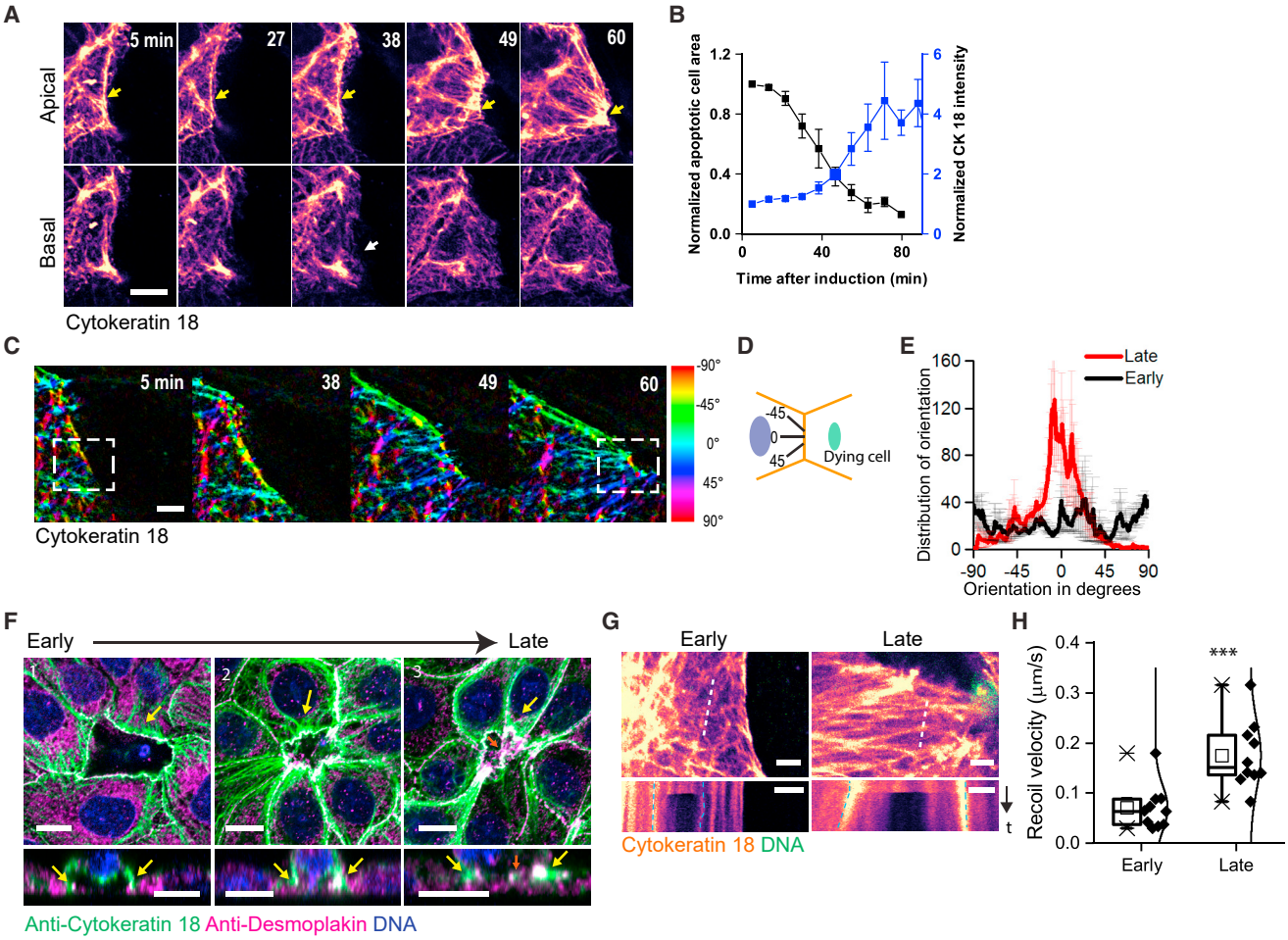

Figure 2. Cytokeratin-18 Rearranges during Apoptotic Cell Extrusion

(A) Confocal images showing the dynamics of mEmerald-cytokeratin 18 within the neighboring cell at apical (top panel) and basal (bottom panel) sections of the cell during extrusion. Yellow arrows denote the interface between the apoptotic cell and the neighboring cell. White arrow highlights cytokeratin-18 in the lamellipodia. See also Figure S2 and Video S2.

(B) Graphs plotting normalized recovery curves of apoptotic cell area (black) and cytokeratin-18 intensity (blue) during cell extrusion (n = 4 independent experiments).

(C) Orientation map of cytokeratin-18 network at different stages of cell extrusion. A white dotted box denotes the region used to measure the orientation.

(D) Illustration describing the orientation of cytokeratin-18 filaments.

(E) Graph plotting the distribution of cytokeratin-18 filament orientation at early (black) and late (red) phases of constriction (n = 4 independent experiments).

(F) Confocal images showing localization of desmosomes (magenta) and cytokeratin-18 (green) during different stages of extrusion. Yellow arrows highlight cytokeratin-18 at the interface. The orange arrow shows the *de novo* junction formation (n = 80 extrusion sites from 4 independent staining experiments).

(G) Confocal images (top) showing the laser ablation of the keratin network at early (~5–10 min after induction) and late (~45–60 min after induction) stages of constriction. The white dotted line shows the site of laser ablation. The kymograph (bottom) shows the recoil of the filaments. The blue dotted line highlights the edge of the keratin filament tracked. See also Video S2.

(H) Recoil velocity of keratin filaments at early and late stages of constriction (n = 10 independent experiments for each condition).

The data in (B), (E), and (H) represent mean ± SEM. Scale bars, 5 μm except for (F) (10 μm). An unpaired two-tailed t test was performed for statistical analysis of (H). ***$p < 0.001$.

proximity to the pre-existing DJs (t = 30; Figures 3A and 3B). This is consistent with a recent study that shows the recruitment of actin to desmoglein 1 at DJs, through cortactin- and Arp2/3-mediated actin polymerization during keratinocyte delamination [10]. Actin and DJs moved together during the early stage of cell extrusion, which is driven by contraction of the actomyosin cable (t = 30; Figures 3A, 3B, S3A, and S3B) [22]. Later, the actin cable spatially deviated from the DJs and shifted toward the basal side of the apoptotic cell (Figures 3A, 3B, and S3C; Video S3). Transverse views and quantification of the z positions of the DJs and the actomyosin cable at different stages of cell extrusion further supported our observations (Figures 3B, 3C, and S3D). Consistent with the analyses of DJs and actin, cytokeratin-18 linked to the DJs also segregated from the actin cable (Figures S3E and S3F; Video S3). Intriguingly, the departure of the actomyosin cable from the DJs coincided with the timing when DJs lost their straightness (Figures 3A and 1B). The quantification of DJ straightness clearly showed that they became wavier

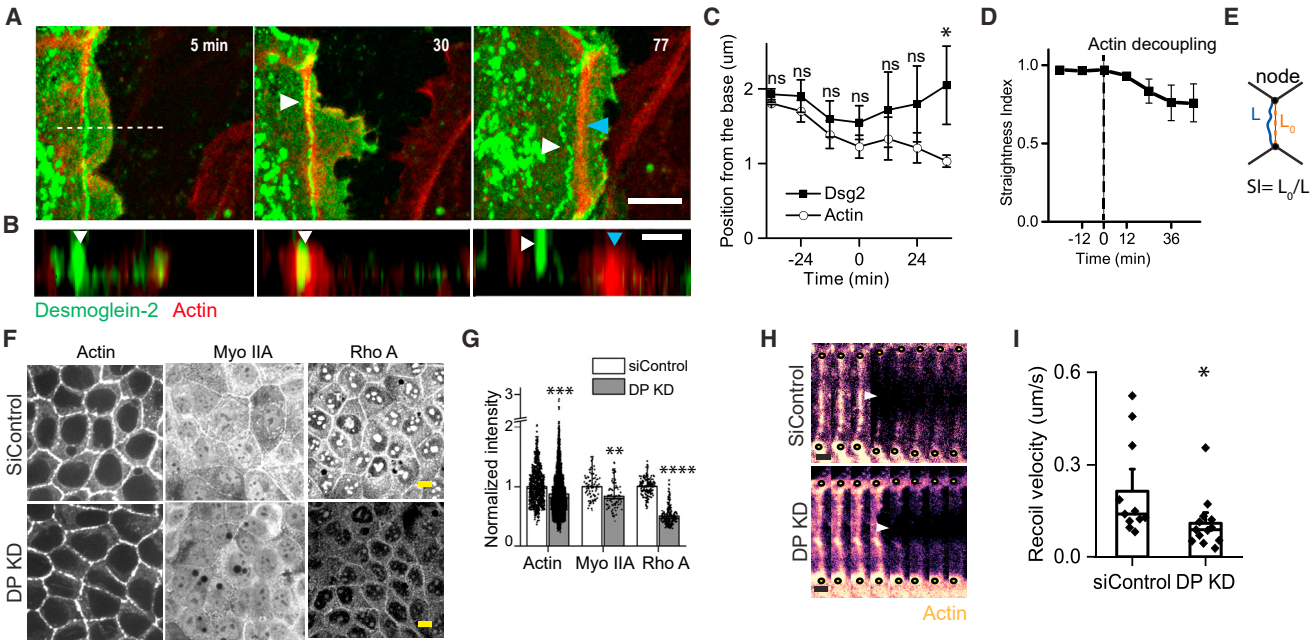

Figure 3. Interplay of Desmosomes and Actomyosin in Apoptotic and Steady-State Junctions

(A) Confocal images showing the localization of actin (blue arrowhead) and desmoglein 2 (white arrowhead) at the apical section of the cell. See also Figure S3 and Video S3.

(B) Transverse view of a neighboring non-dying cell along the white dotted line highlighted in (A). Blue and white arrowheads point to actin cable and desmoglein 2 at DJs, respectively (n = 7 independent experiments).

(C) Quantification of the relative positions of actin and desmoglein 2 at different phases of extrusion (n = 5 independent experiments). t = 0 min denotes the time when actin deviates from DJs.

(D) The changes of straightness index (SI = junctional node displacement [L_0]/path length [L]) of DJs during extrusion. The dotted line t = "0" denotes the time when actin decoupled from DJs (n = 5 independent experiments).

(E) Illustration showing the definition of the straightness index.

(F) Confocal images showing junctional contractile machinery, including actin, myosin IIA, and RhoA, in siControl and DP-depleted MDCK monolayers.

(G) Graph showing the relative level of actin, myosin IIA, and RhoA in scrambled control and DP-depleted junctions. The level of DP-depleted junctions was normalized to the average of the corresponding siControl junctions (actin: n = 861 junctions for siControl and 1,205 junctions for DP KD; MyoII: n = 141 for SiControl and 219 for DP KD junctions; RhoA: n = 175 for SiControl and 211 for DP KD junctions from 3 independent experiments, respectively). See also Figure S3.

(H) Time-lapse images showing actin (Lifeact-Ruby) in both siControl and DP-depleted junctions, before and after junctional ablation, respectively. The yellow dot indicates the position of the junctional node. The white arrowhead shows the site of laser ablation. The time interval between frames is 2.2 s. See also Video S4.

(I) Recoil velocity after laser ablation at intercellular junctions in siControl and DP-depleted monolayers (n = 12 for siControl and 16 for DP KD from 3 independent experiments, respectively).

The data in (C), (D), (G), and (I) represent mean ± SEM. A paired t test was used for statistical analysis of (C). Unpaired two-tailed t tests were performed for statistical analysis of (G) and (I), respectively. *p < 0.05; **p < 0.01; ****p < 0.0001. Scale bars, 10 μm except (B) and (H) (2 μm).

upon decoupling of the actin cable (Figures 3D and 3E), suggesting a release of junctional tension [23] at DJs. Our observations prompted us to speculate that DJs and actomyosin contractility are somehow coupled during apoptotic cell extrusion and in native cell-cell junctions outside of extrusion.

Desmosome-Depleted Junctions Have Aberrant Junctional Actomyosin Networks and Weakened Junctional Tension

To test this hypothesis, we altered desmoplakin (DP) levels by using short interfering RNA (siRNA) and assessed the factors related to junctional tension in a monolayer that was not undergoing apoptosis (Figures S3G and S3H). First, we found that the levels of actin, non-muscle myosin IIA, and RhoA were all lower in siRNA-mediated DP knockdown (KD) monolayers than in scrambled control (Figures 3F and 3G), suggesting that DP depletion was associated with aberrant junctional actomyosin networks and contractility. This was further supported by measurements of the junction-to-cytoplasm ratios of myosin IIA and RhoA in control and knockdown monolayers (Figure S3I). Our results are in agreement with the defective junctional actomyosin networks observed during the depletion of desmoglein 1 from tissue monolayers [10], indicating that depletion of desmosome components leads to an inability to retain the contractile machinery. This may arise from defects in the shuttling of myosin II between its junctional and cytoplasm pools or in myosin II activation [24, 25]. We then performed laser ablation to characterize changes in junctional tension within the monolayer [23] (Figure 3H; Video S4). The initial recoil velocity after laser ablation (STAR Methods) is a good approximation of the junctional tension before ablation [26]. DP-depleted monolayers showed a significantly lower junctional tension as compared to

control monolayers (Figures 3H and 3I), which is in agreement with a recent report that demonstrated lower junctional force upon desmosome depletion [10, 25]. It is important to note that tension levels in the non-apoptotic monolayer (Figure 3I) are lower than the tension at the junctions between apoptotic and neighboring cells (Figures S3J–S3L; Video S4). Together, our results show that DJs directly or indirectly influence actomyosin contractility and this, in turn, affects junctional tension within a tissue. This coupling could also affect dynamic cellular processes, including apoptotic cell extrusion.

Desmosomes Are Crucial for Successful Apoptotic Cell Extrusion

To further investigate the functional significance of DJs, we studied apoptotic cell extrusion in desmoplakin-depleted monolayers. LifeAct-Ruby was expressed to visualize actin distribution and cell shape (Figure 4A). A few cases of extrusion event (5%; n = 70) were associated with a tissue-tearing phenotype at the interface between the apoptotic and neighboring non-dying cells (Figure 4B). In the non-tearing event, more than half of the apoptotic cells (51%; n = 70) showed defective extrusion in DP-depleted monolayers, whereas in the control tissue, all cells (n = 70) were successfully extruded within 2 h (Figures 4C and S4A). In the case of failed extrusion, the majority of cells showed defects in both basal *de novo* DJ formation and apical constriction (black in Figure 4C). The failure of *de novo* DJ formation after desmoplakin depletion supports the molecular clamp model of desmosome function to hold cell-cell junction together in early adhesions that was described previously [27]. We defined an apical constriction defect as a failure in the closure of the apical section of the cell within 2 h. Occasionally, this failure was associated with a lack of persistent constriction resulting in a slight expansion of the cell area after the initial constriction (Figure S4C). Moreover, there was a lack of junctional actin accumulation at the interface between apoptotic and neighboring cells in desmoplakin-depleted monolayers compared to controls (blue arrowhead in Figures 4A, S4B, and S4C). A fraction of the failed extrusion cases showed only the apical constriction defect (Figures 4C, gray, and S4D), and these defects could be explained by the effects of DJs on desmosome-junctional actin interactions [10] and nearby cytokeratin 8/18 filaments [28–30]. We further noticed similar defects related to cell extrusion and tissue integrity in both less-dense and highly dense tissues (Figures S4E and S4F). To complement our DP knockdown experiments, we used a monolayer overexpressing the dominant-negative form of desmoplakin (DPNTP tagged to EGFP) that prevents keratin filament linkage to the desmosomal cadherins [25, 31]. Extrusion defects, including junctional tearing and delayed extrusion, were observed (Figures S4G–S4I; Video S4), which were similar to those observed in DP KD monolayers. We reasoned that lower contractility in the DP KD and DPNTP monolayers, in part, led to such extrusion defects. To test this further, we supplemented the DP KD monolayers with the RhoA activator, CN03, before the induction of extrusion and found that the defective extrusion phenotype was rescued (Figures 4D and 4E). To further delineate the effects of desmosome at the apoptotic-non-apoptotic cell interface, we followed a mosaic approach to overexpress the desmoplakin mutant, DPNTP-FLAG-EGFP, either in the dying cell or in the neighboring cells (Figures S4J and S4K). When a wild-type cell was surrounded by DPNTP cells, both junctional tearing and delayed extrusion were observed, which is analogous to the phenotypes observed in DP KD and DPNTP monolayers. However, when DPNTP was overexpressed in a dying cell surrounded by wild-type cells, we observed delayed extrusion but no tissue tearing. We speculate that apoptosis-induced tissue tearing in DP-depleted tissue depends on the pre-stress of tissue and/or an indirect effect of DP depletion, including a decrease of E-cadherin adhesion through a reduction of junctional tension. Taken together, we conclude that desmosomes play a critical role in the maintenance of tissue contractility to support efficient extrusion processes.

In this study, we reported the importance of DJs in mediating apoptotic cell extrusion. In contrast to E-cadherins, pre-existing DJs that originally link apoptotic cell and neighboring non-dying cells stay intact, even during the formation of *de novo* DJs between non-dying cells beneath the apoptotic cell. These observations suggest that there are two DJs at the late phase of apoptotic cell extrusion and that mechanical coupling of the tissue is maintained throughout cell extrusion. When DJs were compromised by depletion of desmoplakin or overexpression of desmoplakin mutants, cell extrusion was compromised, likely as a consequence of a defect in apical constriction and/or defective *de novo* DJ formation (Figure 4F). This supports the idea that DJs influence actomyosin contractility, which was subsequently confirmed by laser ablation experiments. Although the mechanism of how desmosomes influence actomyosin contractility is still not fully understood, we speculate that this could be through a mechanical and/or a biochemical link between the two cellular components.

The close proximity of DJs, associated intermediate filaments, and the actomyosin cable may mechanically link the actomyosin cable and desmosomes, either with or without cytoskeletal cross-linkers [10, 32]. A recent study reported a physical coupling between desmoglein 1 and actin via cortactin during skin differentiation, which in turn increases junctional tension in the tissue [10]. We speculate that desmoglein 2 may take part in similar mechanisms, coupling actomyosin with DJs during processes such as extrusion. This coupling is supported by our data showing that the shape of the DJs became more tortuous after the actomyosin cable departs from them during cell extrusion. Recent reports have shown how intermediate filaments that anchor at DJs regulate the contractility in proximate actin structures without a direct mechanical link but through biochemical signaling. For instance, intermediate filaments directly sequester myosin [28] and regulatory elements [29] as well as indirectly control the microtubule networks that harbor Rho guanine nucleotide exchange factors (GEFs) [30]. As extrusion is known to occur in multiple settings, including physiological processes, developmental events, oncogenesis, and bacterial pathogenesis [4, 33–35], we further speculate that the defective junctions we observed in desmoplakin-depleted tissues affects actomyosin contractility and/or apoptotic cell extrusion and could lead to pathological conditions. It will be interesting to study whether such extrusion defects are found in diseases and whether known mutations in both desmosomes and

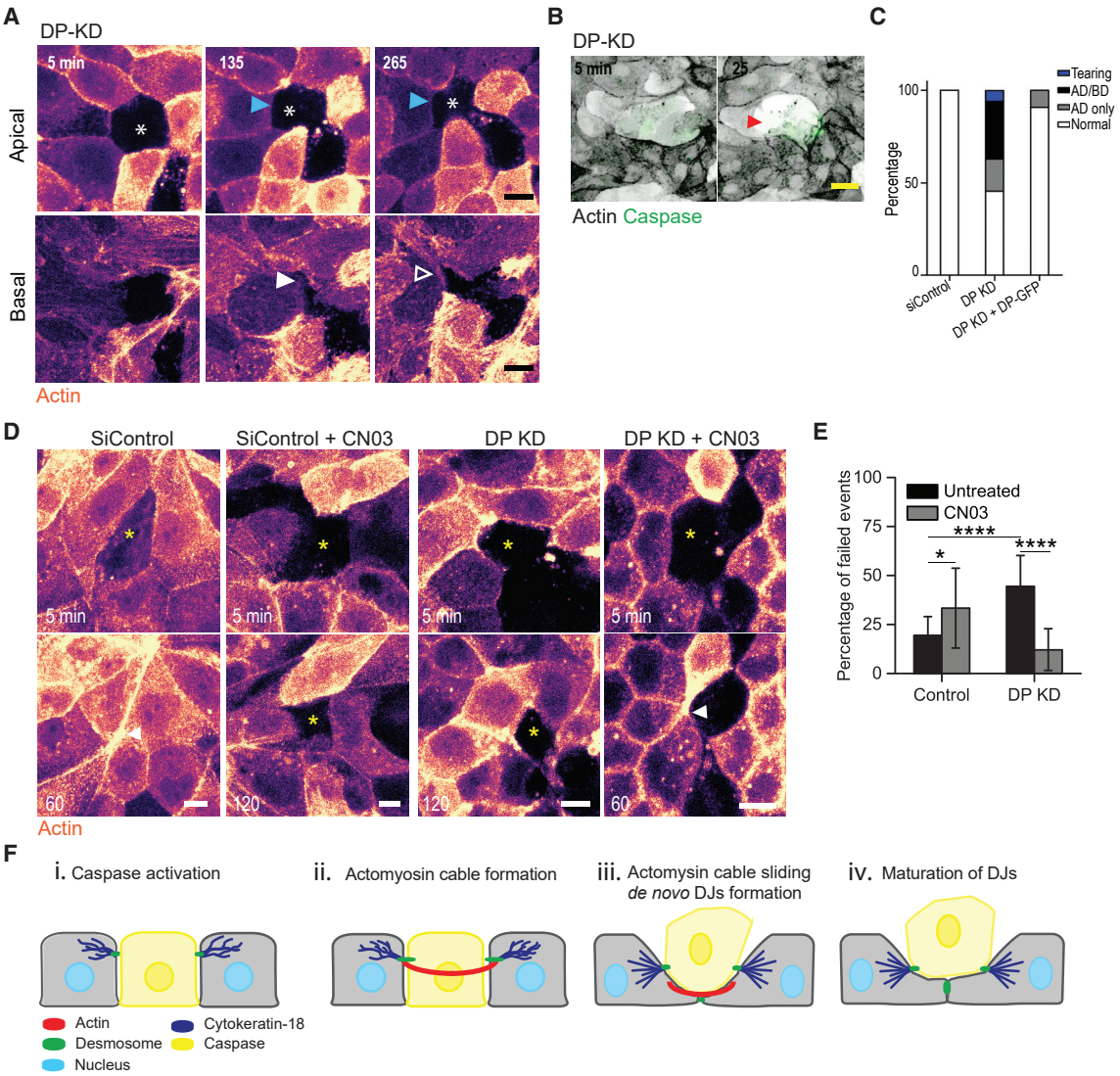

Figure 4. Desmosome Depletion Compromises Apoptotic Cell Extrusion

(A) Confocal images of LifeAct-Ruby (orange) showing apoptotic cell extrusion in DP-depleted tissue at apical (top panel) and basal (bottom panel) sections of the cell. Asterisks and white arrowheads denote the defects in both apical constriction and *de novo* cell-cell junction formation at the basal section, respectively. Blue arrowhead shows the defect of actin accumulation at the interface. See also Figures S3 and S4.

(B) Confocal images showing the junctional tearing phenotype at the apoptotic-non-dying cell interface in DP-depleted monolayers. The red arrowhead highlights a gap in tissue. See also Figure S4 and Video S4.

(C) The fraction of different modes of extrusion in siControl, DP-depleted, and rescue conditions, including AD/BD (apical and basal defects), AD only (apical defect only), and normal conditions. "Normal" denotes a successful extrusion event following apical constriction and *de novo* cell-cell junction formation. n = 70 extrusion events from 6 independent experiments for both siControl and DP KD conditions; n = 11 from 3 independent experiments for rescue condition. See also Figure S4.

(D) Confocal images of LifeAct-Ruby (orange) showing representative phenotypes of siControl and DP-depleted monolayers with or without CN-03 pre-treatment. Yellow asterisks and white arrowheads denote the dying cell and completed extrusion, respectively.

(E) Graph showing fraction of failed extrusion events in siControl and DP KD monolayers with or without CN-03 pre-treatment (n = 50 for siControl and 47 for DP KD from 4 independent experiments, respectively).

(F) An illustration summarizing our findings on the interplay between desmosomes, cytokeratin-18, and actin during apoptotic cell extrusion.

The data from (E) represent mean ± SEM. Two-way ANOVA was used for statistical analysis of (E). *$p < 0.05$; ****$p < 0.0001$. Scale bars, 10 μm.

cytokeratin components can exacerbate diseases such as inflammatory bowel disease (IBD) and cardiomyopathies [36]. It would be important to note that desmoplakin depletion does not induce hyperplasia in the intestinal epithelium [37], suggesting there could be unknown compensatory mechanisms to remove unwanted cells in some contexts. In conclusion, we showed that the coupling of the interface between dying and non-dying cells through desmosomes is required for maintaining epithelial sheet integrity during apoptotic cell extrusion.

STAR★METHODS

Detailed methods are provided in the online version of this paper and include the following:

- KEY RESOURCES TABLE
- LEAD CONTACT AND MATERIALS AVAILABILITY
- EXPERIMENTAL MODEL AND SUBJECT DETAILS
- METHOD DETAILS
  - Plasmids, Si RNA and antibodies
  - Cell culture and transfection
  - siRNA mediated knockdown and validation
  - Laser-based apoptosis induction assay
  - Killer red-based apoptosis induction assay
  - Immunofluorescence and live imaging
  - FRAP and Photoconversion
  - Laser ablation
  - Drug treatment
  - Image processing and quantification
  - Interface intensity, cell spread area and Z position
  - FRAP and photoconversion
  - Straightness index
  - Orientation analysis
  - Junctional Actin, Myosin IIA, and RhoA
  - Movement of actin and Dsg2 puncta
  - Actin decoupling
  - Junctional perturbation studies
  - Recoil velocity
- QUANTIFICATION AND STATISTICAL ANALYSIS
- DATA AND CODE AVAILABILITY

SUPPLEMENTAL INFORMATION

Supplemental Information can be found online at https://doi.org/10.1016/j.cub.2020.01.002.

ACKNOWLEDGMENTS

This work is supported by Singapore Ministry of Education Tier 2 grant (MOE2015-T2-1-116 to Y.T.), USPC-NUS collaborative program (to Y.T and B.L.), and the Agence Nationale de la Recherche "MechanoAdipo" (ANR-17-CE13-0012) and the "Labex Who Am I"? (ANR-11-LABX-0071). We are grateful to Pakorn Kanchanawong for sharing the Michael Davidson collection of plasmids, David. N. Garrod for sharing the desmoglein 2 plasmids, and James W. Nelson for sharing the MDCK Lifeact Ruby and mCherry E-Cadherin cell lines. The authors would like to thank Ong Hui Ting for discussions and help on various aspects of image processing. The authors would like to thank the MBI science communication core's Andrew Wong and Sruthi Jagannathan for editing the manuscript and Melanie Lee for the illustrations. We also thank Virgile Viasnoff, G.V. Shivashankar, and members in the Toyama lab for helpful discussions.

AUTHOR CONTRIBUTIONS

All authors designed the research. M.T. and Y.T. wrote the manuscript. M.T. performed all the experiments and analyses. Y.T. oversaw the project. All authors discussed the results and commented on the manuscript.

DECLARATION OF INTERESTS

The authors declare no competing interests.

Received: May 23, 2018
Revised: October 22, 2019
Accepted: January 2, 2020
Published: January 30, 2020

REFERENCES

1. Rosenblatt, J., Raff, M.C., and Cramer, L.P. (2001). An epithelial cell destined for apoptosis signals its neighbors to extrude it by an actin- and myosin-dependent mechanism. Curr. Biol. *11*, 1847–1857.
2. Kuipers, D., Mehonic, A., Kajita, M., Peter, L., Fujita, Y., Duke, T., Charras, G., and Gale, J.E. (2014). Epithelial repair is a two-stage process driven first by dying cells and then by their neighbours. J. Cell Sci. *127*, 1229–1241.
3. Kocgozlu, L., Saw, T.B., Le, A.P., Yow, I., Shagirov, M., Wong, E., Mège, R.M., Lim, C.T., Toyama, Y., and Ladoux, B. (2016). Epithelial cell packing induces distinct modes of cell extrusions. Curr. Biol. *26*, 2942–2950.
4. Teng, X., Qin, L., Le Borgne, R., and Toyama, Y. (2017). Remodeling of adhesion and modulation of mechanical tensile forces during apoptosis in Drosophila epithelium. Development *144*, 95–105.
5. Michael, M., Meiring, J.C.M., Acharya, B.R., Matthews, D.R., Verma, S., Han, S.P., Hill, M.M., Parton, R.G., Gomez, G.A., and Yap, A.S. (2016). Coronin 1B reorganizes the architecture of F-actin networks for contractility at steady-state and apoptotic adherens junctions. Dev. Cell *37*, 58–71.
6. Lubkov, V., and Bar-Sagi, D. (2014). E-cadherin-mediated cell coupling is required for apoptotic cell extrusion. Curr. Biol. *24*, 868–874.
7. Grieve, A.G., and Rabouille, C. (2014). Extracellular cleavage of E-cadherin promotes epithelial cell extrusion. J. Cell Sci. *127*, 3331–3346.
8. Weber, G.F., Bjerke, M.A., and DeSimone, D.W. (2012). A mechanoresponsive cadherin-keratin complex directs polarized protrusive behavior and collective cell migration. Dev. Cell *22*, 104–115.
9. Gautrot, J.E., Wang, C., Liu, X., Goldie, S.J., Trappmann, B., Huck, W.T., and Watt, F.M. (2012). Mimicking normal tissue architecture and perturbation in cancer with engineered micro-epidermis. Biomaterials *33*, 5221–5229.
10. Nekrasova, O., Harmon, R.M., Broussard, J.A., Koetsier, J.L., Godsel, L.M., Fitz, G.N., Gardel, M.L., and Green, K.J. (2018). Desmosomal cadherin association with Tctex-1 and cortactin-Arp2/3 drives perijunctional actin polymerization to promote keratinocyte delamination. Nat. Commun. *9*, 1053.
11. Godsel, L.M., Hsieh, S.N., Amargo, E.V., Bass, A.E., Pascoe-McGillicuddy, L.T., Huen, A.C., Thorne, M.E., Gaudry, C.A., Park, J.K., Myung, K., et al. (2005). Desmoplakin assembly dynamics in four dimensions: multiple phases differentially regulated by intermediate filaments and actin. J. Cell Biol. *171*, 1045–1059.
12. Wallis, S., Lloyd, S., Wise, I., Ireland, G., Fleming, T.P., and Garrod, D. (2000). The α isoform of protein kinase C is involved in signaling the response of desmosomes to wounding in cultured epithelial cells. Mol. Biol. Cell *11*, 1077–1092.
13. Cirillo, N., Lanza, M., De Rosa, A., Cammarota, M., La Gatta, A., Gombos, F., and Lanza, A. (2008). The most widespread desmosomal cadherin, desmoglein 2, is a novel target of caspase 3-mediated apoptotic machinery. J. Cell. Biochem. *103*, 598–606.
14. Weiske, J., Schöneberg, T., Schröder, W., Hatzfeld, M., Tauber, R., and Huber, O. (2001). The fate of desmosomal proteins in apoptotic cells. J. Biol. Chem. *276*, 41175–41181.
15. Lanza, A., and Cirillo, N. (2007). Caspase-dependent cleavage of desmoglein 1 depends on the apoptotic stimulus. Br. J. Dermatol. *156*, 400–402.
16. Nava, P., Laukoetter, M.G., Hopkins, A.M., Laur, O., Gerner-Smidt, K., Green, K.J., Parkos, C.A., and Nusrat, A. (2007). Desmoglein-2: a novel regulator of apoptosis in the intestinal epithelium. Mol. Biol. Cell *18*, 4565–4578.

17. Cirillo, N., Femiano, F., Gombos, F., and Lanza, A. (2007). Metalloproteinase 9 is the outer executioner of desmoglein 3 in apoptotic keratinocytes. Oral Dis. *13*, 341–345.
18. Yulis, M., Quiros, M., Hilgarth, R., Parkos, C.A., and Nusrat, A. (2018). Intracellular desmoglein-2 cleavage sensitizes epithelial cells to apoptosis in response to pro-inflammatory cytokines. Cell Death Dis. *9*, 389.
19. Gupta, M., Sarangi, B.R., Deschamps, J., Nematbakhsh, Y., Callan-Jones, A., Margadant, F., Mège, R.M., Lim, C.T., Voituriez, R., and Ladoux, B. (2015). Adaptive rheology and ordering of cell cytoskeleton govern matrix rigidity sensing. Nat. Commun. *6*, 7525.
20. Kajita, M., Sugimura, K., Ohoka, A., Burden, J., Suganuma, H., Ikegawa, M., Shimada, T., Kitamura, T., Shindoh, M., Ishikawa, S., et al. (2014). Filamin acts as a key regulator in epithelial defence against transformed cells. Nat. Commun. *5*, 4428.
21. Price, A.J., Cost, A.L., Ungewiß, H., Waschke, J., Dunn, A.R., and Grashoff, C. (2018). Mechanical loading of desmosomes depends on the magnitude and orientation of external stress. Nat. Commun. *9*, 5284.
22. Chen, T., Callan-Jones, A., Fedorov, E., Ravasio, A., Brugués, A., Ong, H.T., Toyama, Y., Low, B.C., Trepat, X., Shemesh, T., et al. (2019). Large-scale curvature sensing by directional actin flow drives cellular migration mode switching. Nat. Phys. *15*, 393–402.
23. Hara, Y., Shagirov, M., and Toyama, Y. (2016). Cell boundary elongation by non-autonomous contractility in cell oscillation. Curr. Biol. *26*, 2388–2396.
24. Priya, R., Gomez, G.A., Budnar, S., Verma, S., Cox, H.L., Hamilton, N.A., and Yap, A.S. (2015). Feedback regulation through myosin II confers robustness on RhoA signalling at E-cadherin junctions. Nat. Cell Biol. *17*, 1282–1293.
25. Broussard, J.A., Yang, R., Huang, C., Nathamgari, S.S.P., Beese, A.M., Godsel, L.M., Hegazy, M.H., Lee, S., Zhou, F., Sniadecki, N.J., et al. (2017). The desmoplakin-intermediate filament linkage regulates cell mechanics. Mol. Biol. Cell *28*, 3156–3164.
26. Toyama, Y., Peralta, X.G., Wells, A.R., Kiehart, D.P., and Edwards, G.S. (2008). Apoptotic force and tissue dynamics during Drosophila embryogenesis. Science *321*, 1683–1686.
27. Vasioukhin, V., Bowers, E., Bauer, C., Degenstein, L., and Fuchs, E. (2001). Desmoplakin is essential in epidermal sheet formation. Nat. Cell Biol. *3*, 1076–1085.
28. Kwan, R., Chen, L., Looi, K., Tao, G.Z., Weerasinghe, S.V., Snider, N.T., Conti, M.A., Adelstein, R.S., Xie, Q., and Omary, M.B. (2015). PKC412 normalizes mutation-related keratin filament disruption and hepatic injury in mice by promoting keratin-myosin binding. Hepatology *62*, 1858–1869.
29. Fujiwara, S., Ohashi, K., Mashiko, T., Kondo, H., and Mizuno, K. (2016). Interplay between Solo and keratin filaments is crucial for mechanical force-induced stress fiber reinforcement. Mol. Biol. Cell *27*, 954–966.
30. Jiu, Y., Peränen, J., Schaible, N., Cheng, F., Eriksson, J.E., Krishnan, R., and Lappalainen, P. (2017). Vimentin intermediate filaments control actin stress fiber assembly through GEF-H1 and RhoA. J. Cell Sci. *130*, 892–902.
31. Kowalczyk, A.P., Bornslaeger, E.A., Borgwardt, J.E., Palka, H.L., Dhaliwal, A.S., Corcoran, C.M., Denning, M.F., and Green, K.J. (1997). The amino-terminal domain of desmoplakin binds to plakoglobin and clusters desmosomal cadherin-plakoglobin complexes. J. Cell Biol. *139*, 773–784.
32. Kadeer, A., Maruyama, T., Kajita, M., Morita, T., Sasaki, A., Ohoka, A., Ishikawa, S., Ikegawa, M., Shimada, T., and Fujita, Y. (2017). Plectin is a novel regulator for apical extrusion of RasV12-transformed cells. Sci. Rep. *7*, 44328.
33. Gu, Y., and Rosenblatt, J. (2012). New emerging roles for epithelial cell extrusion. Curr. Opin. Cell Biol. *24*, 865–870.
34. Kajita, M., Hogan, C., Harris, A.R., Dupre-Crochet, S., Itasaki, N., Kawakami, K., Charras, G., Tada, M., and Fujita, Y. (2010). Interaction with surrounding normal epithelial cells influences signalling pathways and behaviour of Src-transformed cells. J. Cell Sci. *123*, 171–180.
35. Teng, X., and Toyama, Y. (2011). Apoptotic force: active mechanical function of cell death during morphogenesis. Dev. Growth Differ. *53*, 269–276.
36. Owens, D.W., Wilson, N.J., Hill, A.J., Rugg, E.L., Porter, R.M., Hutcheson, A.M., Quinlan, R.A., van Heel, D., Parkes, M., Jewell, D.P., et al. (2004). Human keratin 8 mutations that disturb filament assembly observed in inflammatory bowel disease patients. J. Cell Sci. *117*, 1989–1999.
37. Sumigray, K.D., and Lechler, T. (2012). Desmoplakin controls microvilli length but not cell adhesion or keratin organization in the intestinal epithelium. Mol. Biol. Cell *23*, 792–799.
38. Schindelin, J., Arganda-Carreras, I., Frise, E., Kaynig, V., Longair, M., Pietzsch, T., Preibisch, S., Rueden, C., Saalfeld, S., Schmid, B., et al. (2012). Fiji: an open-source platform for biological-image analysis. Nat. Methods *9*, 676–682.
39. Püspöki, Z., Storath, M., Sage, D., and Unser, M. (2016). Transforms and operators for directional bioimage analysis: a survey. Adv. Anat. Embryol. Cell Biol. *219*, 69–93.
40. Fonck, E., Feigl, G.G., Fasel, J., Sage, D., Unser, M., Rüfenacht, D.A., and Stergiopulos, N. (2009). Effect of aging on elastin functionality in human cerebral arteries. Stroke *40*, 2552–2556.
41. Wang, Y.-H., Hariharan, A., Bastianello, G., Toyama, Y., Shivashankar, G.V., Foiani, M., and Sheetz, M.P. (2017). DNA damage causes rapid accumulation of phosphoinositides for ATR signaling. Nat. Commun. *8*, 2118.
42. Meijering, E., Dzyubachyk, O., and Smal, I. (2012). Methods for cell and particle tracking. Methods Enzymol. *504*, 183–200.

STAR★METHODS

KEY RESOURCES TABLE

REAGENT or RESOURCE	SOURCE	IDENTIFIER
Antibodies		
Anti-Cytokeratin 18 [C04]	Abcam	Cat#ab668 RRID: AB_305647
Anti-Desmoplakin [H300]	Santa Cruz Biotechnology	Cat#sc-33555 RRID: AB_2246069
Anti-Myosin 2A	Sigma-Aldrich	Cat#M8064 RRID: AB_260673
Anti-RhoA [26C4]	Santa Cruz Biotechnology	Cat# sc-418, RRID: AB_628218
Chemicals, Peptides, and Recombinant Proteins		
Alexa Fluor 647 Phalloidin	Invitrogen	Cat#A22287
Nuc View 488 Caspase-3 assay kit	Biotium	Cat#30029
Nuc View 530 Caspase-3 assay Kit	Biotium	Cat#10406
Go 6976	Abcam	Cat# ab141413
Rho Activator II	Cytoskeleton	Cat#CN03
Cell Tracker Deep red	Invitrogen	Cat# C34565
Critical Commercial Assays		
Alamar blue cell viability reagent	Invitrogen	Cat#DAL1025
Experimental Models: Cell Lines		
MDCK	James Nelson lab	ATCC RRDI: CVCL_0422
MDCK-LifeAct Ruby	James Nelson lab	N/A
MDCK-Myosin Light Chain-GFP	James Nelson lab	N/A
MDCK-mCherry-E-cadherin	James Nelson lab	N/A
Oligonucleotides		
Canine Desmoplakin smart pool siRNA: 5′GGAAGAAGCTGGAGGACGA3′, 5′AGGCGGAGCTGGACGGAAA3′, 5′CTACAGAACTGCTCGGATT3′, 5′GAAGATGAGAAGCGAAGAA3′	This paper	Dharmacon Inc., XM_545329
Canine siControl 5′UGGUUUACAUGUCGACUAA3′	This paper	Dharmacon Inc.
Recombinant DNA		
mEmerald-Cytokeratin 18	Michael Davidson collection (Pakorn Kanchanawong lab)	N/A
mem-Killer Red	Michael Levin (unpublished)	Addgene plasmid#45761
DP NTP-FLAG-EGFP	This paper	subcloned from Addgene plasmid#32398 [31]
DP-GFP	[11]	Addgene plasmid #322227
Dendra-2-Cytokeratin 18	Michael Davidson collection (Pakorn Kanchanawong lab)	Addgene plasmid #57726
mCherry-PLC ò-PH	[37]	Michael Sheetz lab
Desmoglein2-FLAG-EGFP	David. N. Garrod lab	N/A
Software and Algorithms		
Fiji	[38]	N/A
Orientation J plugin Fiji	[39, 40]	N/A
Recoil Velocity, MATLAB	[23]	Yusuke Toyama lab
Actin junctional intensity, MATLAB	Mechanobiology image processing core	N/A
Other		
Grided glass dish, μ-Dish	Ibidi	Cat#81168

LEAD CONTACT AND MATERIALS AVAILABILITY

Further information and requests for resources and reagents should be directed to and will be fulfilled by the Lead Contact, Yusuke Toyama (dbsty@nus.edu.sg). This study did not generate new unique reagents.

EXPERIMENTAL MODEL AND SUBJECT DETAILS

Madin-Darby Canine Kidney Epithelium (*Canis familiaris* (dog), female, normal epithelium) based cell lines were used for different experiments in this study. MDCK stable lines overexpressing Myosin Light Chain-GFP, Lifeact Ruby, mCherry-E-cadherin were kindly provided by Prof. James Nelson. MDCK lines were maintained in high glucose DMEM containing Penicillin-Streptomycin (50 U/ml), 10% FCS and geniticin (for maintenance of stable lines) at 37°C in an incubator with 95% humidity and 5% CO_2.

METHOD DETAILS

Plasmids, Si RNA and antibodies

The plasmids, mEmerald-Cytokeratin 18 (Michael Davidson collection), Desmoglein-2-FLAG-EGFP (Prof. David. N. Garrod), mCherry-PLC ò-PH (Prof. Michael Sheetz [41]), mem-killer red (Addgene, 45761), DP NTP-FLAG-EGFP (subcloned from Addgene [31]), DP-GFP (Addgene [11]) and Dendra-2-cytokeratin 18 (Michael Davidson collection) were used in this study. The custom smartpool siRNA against Desmoplakin (XM_545329, 5′GGAAGAAGCTGGAGGACGA3′, 5′AGGCGGAGCTGGACGGAAA3′, 5′CTACAGAACTGCTCGGATT3′, 5′GAAGATGAGAAGCGAAGAA3′) and siControl (5′UGGUUUACAUGUCGACUAA3′) were procured from Dharmacon Inc. Anti-Cytokeratin 18 (ab668, Abcam), Anti-desmoplakin (sc-33555, Santa Cruz), Anti-Myosin 2A (8064, Sigma), and Phalloidin (Invitrogen), Anti-RhoA (26C4, Santa Cruz) were used in different experiments of this study.

Cell culture and transfection

MDCK cells (10^5) were transiently transfected with mEmerald-Cytokeratin-18 plasmid using Lipofectamine 2000 (1:2). Cells and Lip-DNA complex were reverse transfected and seeded into a glass-bottomed dish (Iwaki, 3931-035). After 48 hours of incubation to enable sufficient incorporation of fluorescent protein into filaments, the dish was imaged using a confocal microscope (Nikon A1R MP). Dsg2-FLAG-EGFP and DP NTP-FLAG-EGFP were imaged 24 hours post-transfection. The Caspase cleavable substrate (Biotium, 2 μM) and nuclear marker (Hoechst 33342, 2 μM) were added to the media prior to imaging. For visualization of membrane along with desmosome dynamics, mCherry-PLC ò-PH was co-transfected along with Dsg2-FLAG-EGFP for 24 hours before laser-based apoptosis induction.

For mosaic experiments, wild-type cells and mutant cells were co-cultured for 24 hours before apoptosis induction. In the first case where a mutant dying cell was surrounded by normal neighbors, WT MDCK cells were transfected with DP NTP-FLAG-EGFP 24 hours before co-culture (mutant cells). Mutant and normal (Lifeact-ruby MDCK) cells were co-cultured in the ratio 1:10 to study extrusion dynamics under this condition. In the second case involving mutant neighbor cells and a normal center cell, the following steps were included. WT MDCK cells were labeled with Cell Tracker Deep red (Invitrogen, C34565) to enable visualization of the center cell (normal dying cell). Lifeact-Ruby MDCK cells were transfected with DPNTP-FLAG-EGFP (mutant neighbors) 48 hours prior to co-culture. The normal and mutant cells were co-cultured in the ratio 1:20 followed by apoptosis induction and time-lapse imaging to monitor extrusion dynamics.

siRNA mediated knockdown and validation

For siRNA transfection, 10^5 cells were subjected to 50 nanomoles of resuspended Desmoplakin smart pool siRNA and Dharmafect reagent. Desmoplakin knockdown was obtained 24 hours respectively post-transfection and validated by western blotting. Rescue experiments were performed by transfection of DP KD cells with EGFP tagged Desmoplakin, 24 hours after the first siRNA transfection. For western blotting, 30 μg of denatured protein lysate containing RIPA buffer was loaded into a 4%–15% Tris-glycine gel and subjected to SDS gel electrophoresis. The protein was transferred into a nitrocellulose membrane, transferred by the wet method and immunoblotted to visualize the protein bands by chemiluminescence. Cell viability after transfection was measured using the alamar blue assay (Invitrogen). ~8000 siRNA transfected cells were seeded in a 96 well plate and incubated for 24 hours followed by incubation in Alamar blue (3 hours). The control monolayer was not pre-treated with a transfection mixture. Absorbance at 600nm and 570 nm were measured after 4 hours. Cell viability was calculated using the following formula.

$$\%\ \text{difference between control and siTransfected} = \frac{(O2 \times A1) - (O1 \times A2)}{(O2 \times P1) - (O1 \times P2)} \times 100$$

O1: Molar Extinction Coefficient of oxidized alamarBlue ^{570nm}
O2: Molar Extinction Coefficient of oxidized alamarBlue^{600nm}
A1: Absorbance of transfected well ^{570nm}
A2: Absorbance of transfected well ^{600nm}

P1: Absorbance of Control ^{570nm}
P2: Absorbance of Control ^{600nm}

Laser-based apoptosis induction assay

UV Laser-based apoptosis induction was performed using a custom laser ablation unit interface with the NikonA1R MP microscope [3]. The targeted nucleus was subjected to a laser power of 10-15 nW for 5 s to induce DNA damage, followed by the initiation of time-lapse imaging.

The results from time-lapse imaging during extrusion using overexpressed fluorescent protein constructs were validated by visualizing the respective endogenous components under fixed conditions. For this, WT MDCK cells were seeded into grided 35mm dishes (Ibidi, 81168). Around 10-12 cells (well-separated) of each grid square were subjected to apoptosis induction, fixed (after 60 minutes of the first apoptosis induction) and immunostained. The aforementioned grid locations were subsequently retrieved and imaged to obtain extrusion sites at different stages of extrusion.

Killer red-based apoptosis induction assay

Killer red-based induction was performed by co-culture of mem-killer red expressing MDCK cells and Dsg2-FLAG-EGFP expressing MDCK cells (ratio- 1:8). WT MDCK cells were transfected with mem-Killer red and Dsg2-FLAG-EGFP independently. The transfection mixture was removed after 4 hours and the monolayer was cultured in media for 24 hours. Further, they were trypsinized and co-cultured for 24 hours followed by imaging. For photoactivation, the green epifluorescence module of the Nikon confocal system was used for 5-7 minutes (100%). This was followed by time-lapse confocal imaging to visualize caspase activation and extrusion dynamics of desmosome thereafter.

Immunofluorescence and live imaging

Cells were fixed in either ice-cold methanol (5 minutes) or 4% paraformaldehyde (20 minutes) in PBS. Fixed confocal imaging was performed using a spinning disk confocal microscope (W1), 100x/1.49 objective. Validation of Dsg2-FLAG-EGFP incorporation into endogenous desmosome was performed by transfection of the plasmid into WT MDCK cells. The samples were fixed after 24 hours, immunostained (anti-desmoplakin) and subjected to confocal imaging. Live confocal imaging was performed using Nikon A1R MP with a 60X Nikon Apo 60x/1.40 oil immersion objective lens at 37°C, 5% CO_2 in a humidified incubation chamber. For high time resolution (Figure S3A) and observation of sub-junctional puncta, time-lapse imaging was performed once every 15 s on a single stack.

FRAP and Photoconversion

Dsg 2-FLAG-EGFP was overexpressed in wild-type MDCK cells. A rectangular ROI, 2*1 μm^2 was defined at the interface. Bleaching was performed using the 488 laser at 20% laser power, scanning speed-8 in the NikonA1R MP microscope. FRAP was performed on junctions under three conditions- static junction (non-apoptotic), early extrusion (Bleaching 5 minutes after induction) and late extrusion (bleaching after the *de novo* junction formation). The Z stack was imaged for 30 minutes post bleaching. For photoconversion experiments, Dendra2-Cytokeratin18 was overexpressed in WT MDCK cells. Photoconversion of green filaments into red was performed at an interface ROI using a 405nm laser. A rectangular ROI 2*1 μm^2 was drawn on the interface of the neighboring cell. Photoconversion was performed using the 405 nm laser line of the Nikon A1R MP, using the following conditions: 5% laser power, scanning speed-8, and two iterations. Laser-based apoptosis induction was performed following this and both red and green channels were imaged for 1 hour.

Laser ablation

The apical sections of the cell, with the highest Lifeact Ruby intensity, were used for junctional ablation. This experiment was performed using the ultraviolet laser ablation system (355 nm, 300 ps pulse duration, 1 kHz repetition rate, PowerChip PNV-0150-100, team photonics) [23]. The ablation parameters were optimized as 120 nW, with an exposure time of 0.3 s. Imaging was performed thereafter, at an interval of 2.2 s for a time frame of 90 s. Keratin filament network ablation was performed, by introducing a line cut (6-8 μm) using the same laser at 75 nW, either 5 minutes (early) or 45-60 minutes (late, after cytokeratin reorientation) after induction of apoptosis (laser-based apoptosis induction assay). For ablation of actin cable during extrusion, apoptosis was induced and time-lapse imaging was set up to monitor extrusion dynamics until actin cable formation. At this stage, a line cut (1-2 μm) across the junction was performed at 100 nW and time-lapse images were acquired at an interval of 2 s to capture recoil of desmosome junctional nodes.

Drug treatment

Cells were pretreated with DMSO control or 1 μM Go6976 (Abcam) for 30 minutes followed by laser-based apoptosis induction. For RhoA hyperactivation, siControl and DP-KD monolayers were first subjected to apoptosis (laser-based apoptosis induction assay) and time-lapse imaging to evaluate extrusion dynamics. The same samples were subsequently incubated with 0.25 $\mu g/ml$ Rho Activator II, CN-03 (Cytoskeleton) for 2 hours at 37°C. The samples were further subjected to apoptosis induction and time-lapse imaging to evaluate extrusion dynamics under hypercontractile conditions.

Image processing and quantification

Image processing and quantification were performed using different plugins in Fiji [38].

Interface intensity, cell spread area and Z position

Quantification of cell spread area and interfacial Lifeact, desmoglein, or cytokeratin 18 intensity was computed by drawing a polygon and line ROI (5 pixels wide) respectively at the dying cell interface and stored using the ROI manager. The basal slices with actin stress fibers were excluded from all datasets to avoid interference from the basal cytoskeleton. The sum of slices projection was used for intensity measurement. Normalized intensity (intensity per unit length at t(n) / intensity per unit length at t(1)) was calculated and plotted as a function of time. The calculation of time taken for extrusion of control and knockdown/mutants were performed similarly.

The Z position of DJ and actin during extrusion was computed by generating the transverse view using the ''Reslice'' function of Fiji. The XY coordinates of the centroid of the junction and actin were obtained and quantified. The position of Dsg2 puncta in relation to the nearest membrane was computed by generating a transverse section using the ''Reslice'' function and the distance of the puncta (green) to the nearest membrane (apical, basal and junctional edges) (red) was measured.

FRAP and photoconversion

For quantification of FRAP, the ROI was changed manually across the time series, after taking into consideration the junctional shortening and the change in bleaching ROI thereof during extrusion. A line (width: 5 pixels) was drawn across the newly defined ROI between the junctions to measure the recovery during different stages of extrusion. The normalized intensity of the photobleached ROI (Recovery = intensity at t(n) / pre-bleaching intensity $_{t(0)}$) was calculated and plotted as a function of time. The photoconverted ROI was changed in the time series, w.r.t the extent of the intensity in the red channel. The intensity was measured using a rectangular ROI. The normalized intensity (normalized intensity $_{=}$ intensity at t(n) / intensity at t(1)) of both the red and green channels was measured and plotted. t(1) indicates the intensity at photoconversion.

Straightness index

Straightness index, a chord-arc ratio (SI = Junctional node displacement L_0 / path length L) was obtained by manual segmentation of the junction at different time points using Fiji, to obtain both the junctional length as well as displacement between the junctional nodes.

Orientation analysis

The orientation of the global Cytokeratin18 network during the progression of extrusion was computed by measuring the structure tensor of the timelapse images. This was performed using the OrientationJ plugin of Fiji [39, 40]. The images in the time series were background subtracted, and rotated parallel to the line connecting the centroids of the dying cell and the neighbor at t_1. The orientation plots and the corresponding angle distribution were obtained. The color survey was generated by setting the three parameters; hue, saturation, and brightness to orientation, the original image and constant respectively. The orientation angles were obtained and plotted as a distribution.

Junctional Actin, Myosin IIA, and RhoA

Junctional actin was computed using a custom MATLAB algorithm. The algorithm performed local thresholding and segmented the junctions, followed by separation of the branched nodes, to enable intensity quantification of individual junctions. The junctional actin was measured by drawing a junctional line ROI (width: 5 pixels).

Junctional myosin IIA and Rho A were quantified manually using a Fiji macro, owing to the poor cytoplasm-junction contrast. The segmentation of the junctional pools of myosin IIA and Rho A were performed manually. The basal sections of the cell were removed, and the apical slices were used to generate a projection (sum of slices), followed by drawing a segmented line ROI (width: 5 pixels) to measure the corresponding intensity. Normalized intensity of DP KD junction (Normalized intensity at J_{KD1} = Intensity at J_{KD1}/ Average intensity of control junctions) was calculated and plotted. To further compute junction to cytoplasm ratio (ratio = Average intensity of junction I_{junc}/ Average intensity of cytoplasm I_{cyto}), a circular cytoplasmic ROI (5 μm diameter, nucleus excluded and adjacent to the corresponding junction) was drawn on the projected image to obtain the cytoplasmic intensity in addition to the junctional intensity obtained as described above. The intensity of DP KD associated junctions was normalized with respect to the normal junctions and plotted.

Movement of actin and Dsg2 puncta

A kymograph was drawn manually along the junction during constriction using Fiji. Tracks of Dsg2 and Lifeact-Ruby pairs were drawn manually. The slope was computed by obtaining the line coordinates and plotted.

Actin decoupling

Time difference (ΔT) is defined as the time lag between a detachment of desmosome in the middle of the junction as compared to the junctional nodes. '0' indicates simultaneous decoupling. The probability density function of ΔT was computed and plotted.

Junctional perturbation studies

An extrusion site where the dying cell is removed from the monolayer within 120 minutes is defined as 'normal'. An extrusion site where the extruding cell remains in the epithelium after 120 minutes of apoptosis induction was defined as 'delayed'. An extrusion site where the extruding cell loses contact with the neighbor cells was defined as 'tearing'.

Recoil velocity

Recoil velocity was computed by tracking the Cartesian coordinates of the junction nodes using MTrackJ plugin in Fiji [42], followed by fitting the calculated distance between nodes into a single/double exponential function. Recoil velocity was calculated as the derivative of the function using a custom made MATLAB algorithm [23].

QUANTIFICATION AND STATISTICAL ANALYSIS

The data indicated are mean ± SEM. The number of independent experiments performed is indicated in figure captions. At least 4 independent biological replicates were performed for each experiment. The statistical details of experiments can be found in the respective figure legends. All datasets passed normality tests before being subjected to statistical tests. Statistical tests were performed using Graphpad Prism and Origin Pro 6.0. Unpaired t test (with Welch correction) (Figures 2H, 3G, 3I, and S3I) and Paired t test (Figure 3C) were used to test the statistical significance.

DATA AND CODE AVAILABILITY

This study did not generate any unique datasets or code. Requests for data and analysis code may be directed to the lead contact, Yusuke Toyama (dbsty@nus.edu.sg).